TU/e EINDHOVEN UNIVERSITY OF TECHNOLOGY

Eindhoven University of Technology

BACHELOR

The urban heat island

Schlepers, T.D.

Award date:
2011

Link to publication

The urban heat island

Tomas Schlepers

R-1795-S

October 2011

Supervisors:
Dr.ir. R.P.J. Kunnen
Prof.dr.ir. G.J.F. van Heijst
Dr.ir. L.P.J. Kamp

Eindhoven university
Faculty of Applied Physics
Turbulence and vortex dynamics

Abstract

In this project the flow induced by a (urban) heat island with background rotation has been studied. This is done experimentally as well as numerically. From the experiments it is shown that there are two regimes in the flow pattern in the fluid characterised by the Rossby number. These regimes are $Ro \ll 1$ and $Ro \gg 1$ with the transition point at $Ro \approx 1$. At small Rossby numbers there is a cylindrical vortex, whereas at large Rossby numbers large convection cells are formed. Around the transition point the flow pattern has a conical shape. The numerical simulations are compared with experiments and it is concluded that the simplifications in the simulations are unrealistic.

Contents

Chapter 1

Preface

In modern day society we cannot ignore the influence of the production of heat of large cities on the climate. This phenomenon, also known as the urban heat island, has drawn the attention of many researchers. This is due to the significance for meteorology. See for example [1, 2, 3].

This heat island is also discovered in nature itself. One of the most familiar examples is the Tibetan Plateau. The table mountain in this region acts as the local heat source which heats the air above, creating interesting weather patterns in this way.

The same principle holds for large cities, which act as local heat sources. This generates a local uplift of air above the city, which in turn causes air to flow towards the city over the ground. Due to the rotation of the earth this circulation of air is deflected and will create vortices. These vortices are examined in this study. As said before it is important to map the different types of phenomena that can occur in these situations, specifically for weather forecasting. With the help of some simplifications it is possible to simulate this localized heat source in a medium in a laboratory. This means that the urban heat island is simplified to a rotating tank filled with water and a heating disc at the bottom. Experiments are done on this model system together with numerical simulations. With the help of the theory a prediction can be given with regard to the different types of behaviour of the flow. This is done in Chapter 2. In Chapter 3 the experimental setup is discussed. Another subject of this chapter will be the discussion on the simulations done on the matter. In Chapter 4 the results from the experiment are presented. This will be done using snapshots from the dye visualisations. Also the outcome of the simulations will be presented in this chapter. In Chapter 5 we draw several conclusions from the results.

Chapter 2

Theory

In this chapter the theoretical background of this flow problem is explained. To simplify the equations of motion the Boussinesq approximation has been applied. This procedure will be discussed in Section 2.1.1, whereas in Section 2.1.2 the influence of rotation is introduced. The dimensionless parameters that describe the flow are mentioned in Section 2.2. With the help of these parameters it is easier to categorize different regimes of flow in the medium. There are several phenomena that occur during the experiments that need explaination at forehand. These phenomena are the Ekman boundary layer, the Taylor-Proudman theorem and the Taylor column. These three items are discussed below in Section 2.3 and in Section 2.4.

2.1   Equations of motion

2.1.1   Equations without rotation

The Navier-Stokes and heat equations for an incompressible fluid can be simplified using the Boussinesq approximation [4, 5]. This approximation states that variations in density are negligible unless they are multiplied with the gravitational acceleration g:

$$\vec{\nabla} \cdot \vec{v} = 0, \tag{2.1a}$$

$$\frac{\partial \vec{v}}{\partial t} + (\vec{v} \cdot \vec{\nabla})\vec{v} = -\vec{\nabla}P + g\alpha T\hat{\vec{z}} + \nu\nabla^2\vec{v}, \tag{2.1b}$$

$$\frac{\partial T}{\partial t} + (\vec{u} \cdot \vec{\nabla})T = \kappa\nabla^2 T. \tag{2.1c}$$

In Equation (2.1) $\vec{v}$ is the velocity with cartesian components v_x, v_y and v_z, P is the pressure and T the temperature. Besides these variables there are several constants like g, which is the gravitational acceleration, α, ν and κ. Here, α is the coefficient of thermal expansion, ν is the kinematic viscosity of the fluid and κ is the thermal diffusivity of the fluid.

2.1.2 Rotation

Since this experiment is performed with background rotation, it is important to be able to predict the effects that are caused by the additional forces due to the rotation. It is possible to deduce these extra forces mathematically but that is not done in this report. For this deduction see [5]. The end result of this excersise is expressed as:

$$\vec{a}_R = \vec{a}_I - 2\vec{\Omega} \times \vec{v}_R - \vec{\Omega} \times (\vec{\Omega} \times \vec{r}_R). \tag{2.2}$$

There are several symbols in Equation (2.2) that need an explaination. The vector $\vec{a}_R$ is the acceleration in the rotating frame of reference, whereas $\vec{a}_I$ is the acceleration in the inertial frame of reference. The same holds for the velocities and positions since $\vec{v}_R$ and $\vec{r}_R$ are the velocity and position in the rotating frame of reference, respectively and $\vec{v}_I$ and $\vec{r}_I$ are the velocity and position in the inertial frame of reference, respectively. The rotating frame of reference is taken as a frame that rotates with an angular frequency of Ω with its z-axis along the axis of rotation. In Equation (2.2) there are two additional terms of acceleration, these are:

$$\text{Coriolis acceleration } \vec{a}_c = 2\vec{\Omega} \times \vec{v}_I, \tag{2.3a}$$

$$\text{Centrifugal acceleration } \vec{a}_{cf} = \vec{\Omega} \times (\vec{\Omega} \times \vec{r}_I). \tag{2.3b}$$

From this result it is possible to rewrite the centrifugal acceleration to a gradient that can be brought into the pressure gradint. This is the modified pressure.

2.2 Dimensionless parameters

It is more convenient to work with dimensionless parameters since they make it easier to determine the significance of the various forces. That is why the equations of motion which were found before are simplified by characteristic length, velocity, time, temperature and pressure scales. The definitions of these characteristic scales and the implementation of these in the governing equations is done in Section 2.2.1. After implementation, some dimensionless quantities can be defined. This is done in Section 2.2.2.

2.2.1 Dimensionless equations of motion

To make the governing equations dimensionless the various quantities need to be made dimensionless. This can be done using the following set of definitions, in which H, U and ΔT are the characteristic length, velocity and temperature scales, respectively and the quantities with bar are the dimensionless parame-

ters.

$$\vec{\bar{x}} = \frac{\vec{x}}{H} \qquad\qquad \bar{t} = \frac{Ut}{H}$$

$$\vec{\bar{u}} = \frac{\vec{u}}{U} \qquad\qquad \bar{\nabla} = H\nabla$$

$$\vec{\bar{T}} = \frac{T}{\Delta T} \qquad\qquad \bar{\nabla}^2 = H^2\nabla^2$$

$$\vec{\bar{p}} = pU^2$$

When these definitions are substituted into Equation (2.1a) the following result is obtained:

$$\bar{\nabla} \cdot \vec{\bar{u}} = 0, \tag{2.4}$$

If the same procedure is repeated with Equation (2.1b) this gives the following expression:

$$\frac{U^2}{H}\frac{\partial \vec{\bar{u}}}{\partial \bar{t}} + \frac{U^2}{H}(\vec{\bar{u}} \cdot \vec{\bar{\nabla}})\vec{\bar{u}} + 2\Omega U \hat{\bar{z}} \times \vec{\bar{u}} = -\frac{U^2}{H}\vec{\bar{\nabla}}\bar{p} + g\alpha\Delta T \bar{T}\hat{\bar{z}} + \frac{U}{H^2}\nu\bar{\nabla}^2\vec{\bar{u}}. \tag{2.5}$$

Equation (2.5) can be simplified to the following form:

$$\frac{\partial \vec{\bar{u}}}{\partial \bar{t}} + (\vec{\bar{u}} \cdot \vec{\bar{\nabla}})\vec{\bar{u}} + \frac{2\Omega H}{U}\hat{\bar{z}} \times \vec{\bar{u}} = -\vec{\bar{\nabla}}\bar{p} + \frac{g\alpha\Delta T H}{U^2}\bar{T}\hat{\bar{z}} + \frac{\nu}{UH}\bar{\nabla}^2\vec{\bar{u}}. \tag{2.6}$$

From Equation (2.6) it is possible to define a characteristic velocity scale U because the maximum speed of a small volume of fluid above the heating disc, with the additional requirement that there is no background rotation, is reached when the convective term $g\alpha\Delta T H/U^2$ equals unity. This gives $U \equiv \sqrt{g\alpha\Delta T H}$.

Finally Equation (2.1c) has to be made dimensionless. This is done by the same procedure with which the preceding two equations were handled. When written in full, this gives the equation:

$$\Delta T\frac{U}{H}\frac{\partial \bar{T}}{\partial \bar{t}} + \frac{U\Delta T}{H}(\vec{\bar{u}} \cdot \vec{\bar{\nabla}})\bar{T} = \frac{\kappa\Delta T}{H^2}\bar{\nabla}^2\bar{T}. \tag{2.7}$$

When the above equation is simplified, the following formula remains:

$$\frac{\partial \bar{T}}{\partial \bar{t}} + (\vec{\bar{u}} \cdot \vec{\bar{\nabla}})\bar{T} = \frac{\kappa}{UH}\bar{\nabla}^2\bar{T}. \tag{2.8}$$

2.2.2 Dimensionless quantities

With the governing equations in dimensionless form it is possible to specify the experiment by a set of dimensionless quantities. The first that will be defined is called the Rayleigh number, which gives the ratio of heat transport by convection and by conduction. This can be seen by its definition:

$$Ra \equiv \frac{g\alpha\Delta T H^3}{\nu\kappa} \tag{2.9}$$

In the above equation H is the height of the fluid. With the help of the Rayleigh number a prediction about the nature of the transportation of heat in the specific fluid can be made. When this number is below a critical value, transport will be mainly due to conduction. When it exceeds this critical value heat transport is primarily in the form of convection.

Another dimensionless quantity that is of importance in this experiment is the Rossby number. The definition of this number can be read from Equation (2.6). This definition is:

$$Ro \equiv \frac{U}{2\Omega H}. \tag{2.10}$$

As can be seen from the definition above, this number compares inertial and Coriolis forces. The last dimensionless quantity that is of importance is the Prandtl number. This number describes the diffusive properties of the fluid. The definition of the Prandtl number is given by:

$$Pr \equiv \frac{\nu}{\kappa} \tag{2.11}$$

2.3 Ekman boundary layer

In this report there will be only a minor discussion about the Ekman boundary layer [6]. Only those subjects that are of importance are mentioned. For a more thorough discussion about this subject see [5]. Those elements of importance ar the Ekman number and the depth of the Ekman boundary layer at different Rossby numbers. The first is a dimensionless number that describes the ratio of the viscous forces to Coriolis forces and is defined as:

$$Ek = \frac{\nu}{\Omega H^2}. \tag{2.12}$$

The depth of the Ekman boundary layer is defined as:

$$\delta_{Ek} = \sqrt{\frac{\nu}{\Omega}}. \tag{2.13}$$

From Equation (2.13) it can be concluded that the thickness of the Ekman boundary layer does not depend on the size of the tank nor on the veocities in the fluid. Another conclusion is that $\delta_{Ek} \backslash H = \sqrt{Ek}$. A remarkable feature of the Ekman boundary layer is that when there is vorticity in the fluid above the boundary layer this gives rise to a vertical transport of fluid depending on the sign of the vorticity. If this is positive there will be upward transport but when it is negative there will be a downward transport of fluid. In this experiment the vorticity will be positive so the transport of fluid will be upward, giving rise to a radial inward flow pattern at the bottom of the tank.

2.4 Taylor-Proudman theorem and the Taylor column

As for the Ekman boundary layer, in this section only the important facts of the Taylor-Proudman theorem and the Taylor column will be discussed. For a more thorough understanding see [5]. First, the Taylor-Proudman theorem will be introduced, after which the Taylor column is explained. Finally the changes due to the influence of the temperature are mentioned. For the Taylor-Proudman theorem to hold, several conditions have to be satisfied. These conditions are:

- The flow must be (quasi-)steady, which means that the time derivative is approxiamtly 0. And the rotational speed has to be high so that the Coriolis force is large in comparison to the inertial terms, which means that this theorem only holds in the regime $Ro \ll 1$,

- The flow must be inviscid, which means that $Ek \ll 1$. This implies that the Taylor-Proudman theorem is not valid near noundaries, where viscosity plays a role.

The essence of the Taylor-Proudman theorem is that vertical variations of the velocity are absent. This means that the flow pattern becomes independent of the vertical position. Due to viscosity this statement does not hold close to the walls. One of the effects of this theorem is the formation of a Taylor column [8]: an object dragged slowly through a rotating fluid transports the fluid above along with it as though it is a single solid object. This is a column above the heating plate in which hot fluid is transported upward due to the positive vorticity that generates a radial inward flow at the bottom of the tank.

Since this experiment is performed with temperature changes, and the Taylor-Proudman theorem does not incorporate temperature gradints, the influence of the temperature has to be taken into account. The name for interaction between a Taylor column and temperature changes is the thermal wind equilibrium [9]. The result of this effect is that vertical gradients of the horizontal velocity components are allowed due to the temperature gradient that originates from the cooling of the fluid. However, the vertical velocity remains independent of the vertical coordinate. In the experiments at $Ro \ll 1$ we thus expect a columnar vortex with positive vorticity, fed by radial inflow near the bottom, transporting hot fluid upward.

Chapter 3

Experimental setup and simulation procedure

In this chapter the experimental setup is discussed, as well as the numerical simulations. In Section 3.1 the experimental setup is presented together with additional information about the operation. In Section 3.2 the simulation procedure is explained.

3.1   Experimental setup

As been said before the setup consists of to a cylindrical tank filled with water which is mounted on a rotating table. The water is heated using a small heating disc at the bottom of the tank. A sketch of this is shown in Figure 3.1.

In Figure 3.1 there are several labels attached to different elements of the setup. These will now be explained. To begin with, A is the cylindrical tank that contains the water. This container is made out of plexiglass and is 17.5 mm thick and has a diameter of 50 cm. In the bottom plate a heating element B is placed. This is a hollow block of copper of diameter 50 mm through which hot water flows. Due to the high thermal conductivity of copper this is a good material to conduct the heat from the hot water towards the large water tank. Since plexiglass has a low thermal conductivity compared to copper, 0.2 W m^{-1} K^{-1} to 401 W m^{-1} K^{-1}, this material is a good insulator for the heat produced by the heating disc. The letters C and D represent the two cameras. Two Logitech webcams are used, one recording from above, the other recording from the side. In this way, both vertical and horizontal motions can be recorded. These webcams are connected to a computer which is mounted under the rotating table E. This computer is accessible through a remote desktop connection with a laptop that is outside the rotating frame. To visualize the flow in the water a dye is used. This dye is injected by hand in the middle of the tank, just above the heating disc. Before the dye is injected the table and heating disc are turned on for some time to establish a steady state situation.
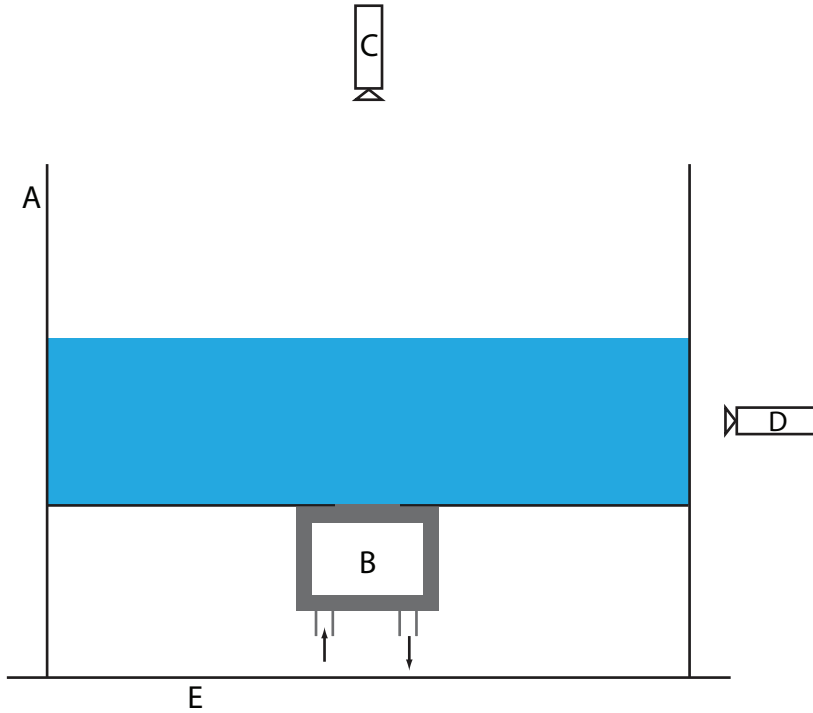
Figure 3.1: Sketch of the experimental setup. Labels will are explained in the text.

This spin-up time is based on the Ekman spin-up time that is defined as [9]:

$$\tau_E = \frac{H}{\sqrt{\nu\Omega}}. \tag{3.1}$$

The largest spin-up time is when the angular frequency is lowest, namely 0.1 rad s^{-1}. Using the known values for H and ν this gives a spin-up time of approximately 6 minutes. This means that the settling time used in this experiment is taken at 20 minutes to be sure a steady state is reached inside the fluid. The tank is aligned with the rotation axis of the table. This means that the centre of the heating disc lies on this rotation axis.

To have a full understanding of the different flow patterns inside the fluid, measurements have been carried out over a wide range of angular frequencies. These frequencies are summarized in Table 3.1. For each measurement series there are more measurements around $Ro \approx 1$. For temperature differences of 5, 10 and 15 K the Rayleigh numbers are 1.36×10^9, 2.72×10^9 and 4.07×10^9, respectively.

To be able to see the temperature dependence of the flow patterns measurements are done at $Ra = 2.72 \times 10^9$ and at $Ra = 4.07 \times 10^9$. For $Ra = 2.72 \times 10^9$ additional measurements have been done at $Ro = 1.06$, $Ro = 1.004$ and at

Table 3.1: Overview of several values of the Rossby number at different angular frequencies and different temperatures, expressed by

$\Omega(\text{rad s}^{-1})$	$Ro(Ra = 1.36 \times 10^9)$	$Ro(Ra = 2.72 \times 10^9)$	$Ro(Ra = 4.07 \times 10^9)$
0	-	-	-
0.1	1.60	2.26	2.77
0.2	0.80	1.13	1.38
0.3	0.53	0.75	0.92
0.4	0.40	0.56	0.69
0.5	0.32	0.45	0.55
0.6	0.27	0.38	0.46
0.7	0.23	0.32	0.40
0.8	0.20	0.28	0.35
0.9	0.18	0.25	0.31
1.0	0.16	0.23	0.28
1.5	0.11	0.15	0.18

$Ro = 0.90$. For $Ra = 4.07 \times 10^9$ the additional considered values are $Ro = 1.11$, $Ro = 1.006$ and $Ro = 0.96$.

3.2 Simulations

The experimental results are compared with numerical simulations. These simulations are done in Comsol multiphysics using the assumption that the fluid flow is axisymmetric. This means that there are no variations in velocity in the azimuthal direction in the rotating frame so the simulation can be done in 2 dimensions. The equations that are used to solve this system are those
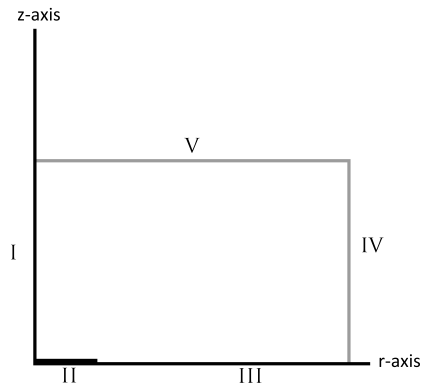

Figure 3.2: Schematic overview of the computational domain used in the numerical simulations.

of Equation (2.4), Equation (2.6) and Equation (2.8). Some of the terms in these equations have to be added as volume forces in Comsol like the Coriolis and convective force. The slice for which the numerical simulation is solved is half a vertical cross-section with on one side the rotation axis and on the other the sidewall. This computational domain is shown in Figure 3.2. To make the simulation work additional boundary conditions are defined. The boundaries on which these conditions act are stated in Figure 3.2. The axis of rotation is indicated by I, the heating disc by II, the rest of the bottom plate by III. The outer wall is indicated with IV and the open boundary with V. The boundary conditions are:

- II, III and IV are rigid, no-slip walls,

- II is given a fixed, constant temperature,

- III and IV are thermal insulators,

- There is a steady outward heat flux at V that depends on the temperature difference between the surroundings and the fluid,

- V is taken to be rigid and stress-free.

To complete the description of the simulation it is necessary to define initial values for the temperature and the velocity field at the start of the experiment. At $t = 0$ s it is assumed the fluid has a constant temperature troughout its volume. The temperature of the fluid is specified by the temperature of the surroundings. The initial values for the velocity field are that all three components of the velocity are zero.

To be able to accurately perform this simulation a fine enough mesh has to be defined. A mesh that is too coarse leads to an unphysical solution. The mesh is made by discretizing the computational domain. This discretizing can be done coarse or fine. When the mesh is made finer the numerical simulation will be more exact but the downfall is a longer calculation time.

To test whether the results are correct or not the mesh can be refined. If the result remains the same this means that the result was correct. If the outcome changes, however, that means that the coarser mesh gave and outcome that was not yet converged to the exact solution and the mesh should be refined until the outcomes no longer differ and the resolution is fine enough. Since the laptop at which the first simulations were made did not have enough memory to achieve correct results, the numerical simulations are performed by dr. Kamp. The results of his numerical simulations were provided to compare them with the actual experimental results.

Chapter 4

Results and discussion

When the Rayleigh number is 2.72×10^9, heat transport in this experimental setup is mainly due to convection. Snapshots are made at different angular velocities Ω to show the flow patterns that can occur. Examples are shown in Figure 4.1. The black lines on the snapshots are guides to the eye to emphasize the flow pattern above the heated disc. From these snapshots a transition between regimes can be identified. Snapshots of the situation without and with very little rotation reveals the formation of large convection cells that fill the domain. An example is shown in Figure 4.1a. When considering the case $Ro \approx 1$ it can be seen that the flow pattern adopts a conical shape. Here, the dye is being transported upwards in a conical pattern that evolves towards a cylindrical vortex for $Ro \ll 1$. This last regime is best seen in Figure 4.1e. Snapshots from the measurement series at $Ra = 4.09 \times 10^9$ are shown in Figure 4.2. As in the previous measurement series these snapshots illustrate the transition between regimes as a function of the Rossby number. The conical shape can be seen in Figure 4.2a. The snapshots at $Ro = 1.11$, $Ro = 1.006$ and $Ro = 0.92$ show the transition from a cone towards a column. From these two measurement series it was decided that additional measurements with a better contrast dye should be made at Ro=0.90 and at Ro=0.15 for Ra=2.72×10^9. For $Ra = 4.09 \times 10^9$ the additional measurements are done at $Ro = 1.11$ and $Ro = 0.18$. For comparison with the simulations of dr. Kamp measurements are also done at $Ro = 0.32$ and $Ro = 0.11$ for $Ra = 1.36 \times 10^9$. These additional measurements are done with a blue dye that enhanced the contrast in the snapshots. This increased contrast made it possible to measure the diameter of the Taylor column when $Ro < 1$. Indicatory snapshots of the measurements with the blue dye are presented in Figure 4.3.

The results of the measurements at $Ra = 1.36 \times 10^9$ are not included in this report since it was not possible to reliably interpret them. In the measurements at both Rossby numbers no clear structures were formed. The only structures that appeared were dipoles that are probably formed due to the retraction of the pipette by hand. It is clear that this is one of the points that can be improved in further investigations.

(a) $Ro = 2.26$

(b) $Ro = 1.13$

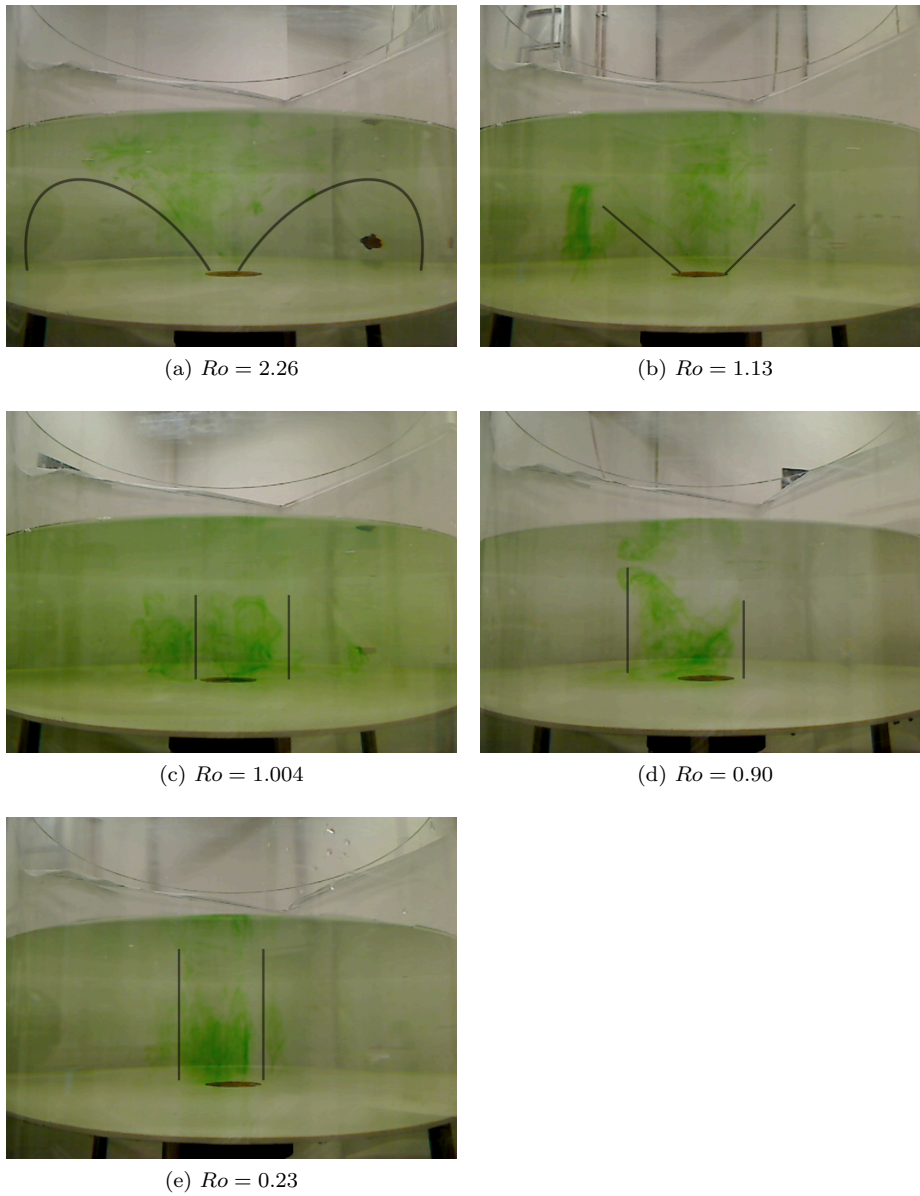(c) $Ro = 1.004$

(d) $Ro = 0.90$

(e) $Ro = 0.23$

Figure 4.1: Snapshots of dye visualisation at $Ra = 2.72 \times 10^9$. Various Rossby numbers are included.

In Figure 4.3 the different flow patterns as described above can be recognized. In Figures 4.3a and 4.3b the conical shape is present above the heating disc. The only conclusion that can be drawn from the experiment regarding the relation between the temperature difference and the slope of the cone is that the slope

(a) $Ro = 1.38$

(b) $Ro = 1.11$

(c) $Ro = 1.006$
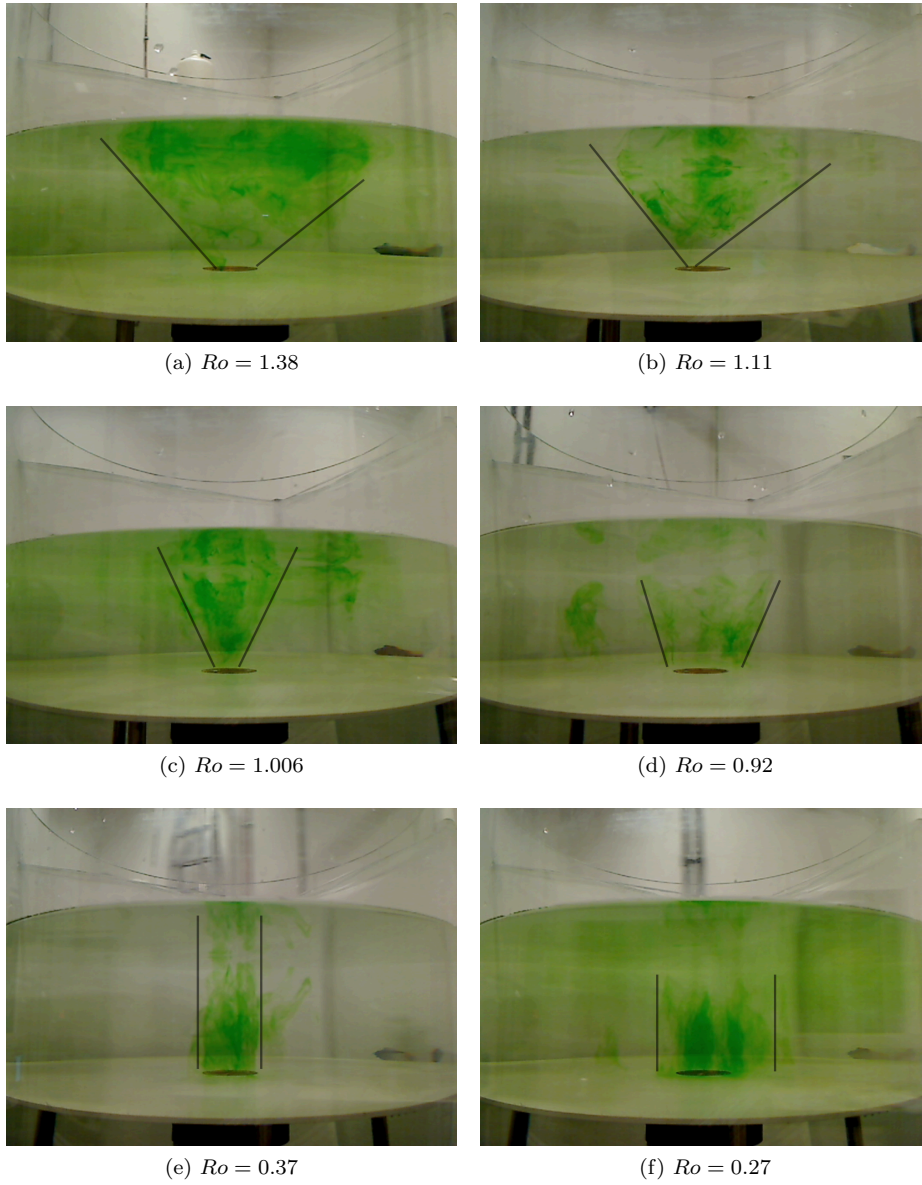
(d) $Ro = 0.92$

(e) $Ro = 0.37$

(f) $Ro = 0.27$

Figure 4.2: Dye visualisation snapshots at $Ra = 4.09 \times 10^9$. Various Rossby numbers are included.

appears to be steeper at higher temperature difference. About the other flow pattern, the Taylor column of Figures 4.3c and 4.3d, quantitative statements can be made. This is due to the fact that the diameter of this column can be measured from the snapshots using the known diameter of the heating disc.

(a) $Ro = 0.90, Ra = 2.72 \times 10^9$

(b) $Ro = 1.10, Ra = 4.09 \times 10^9$

(c) $Ro = 0.15, Ra = 2,72 \times 10^9$
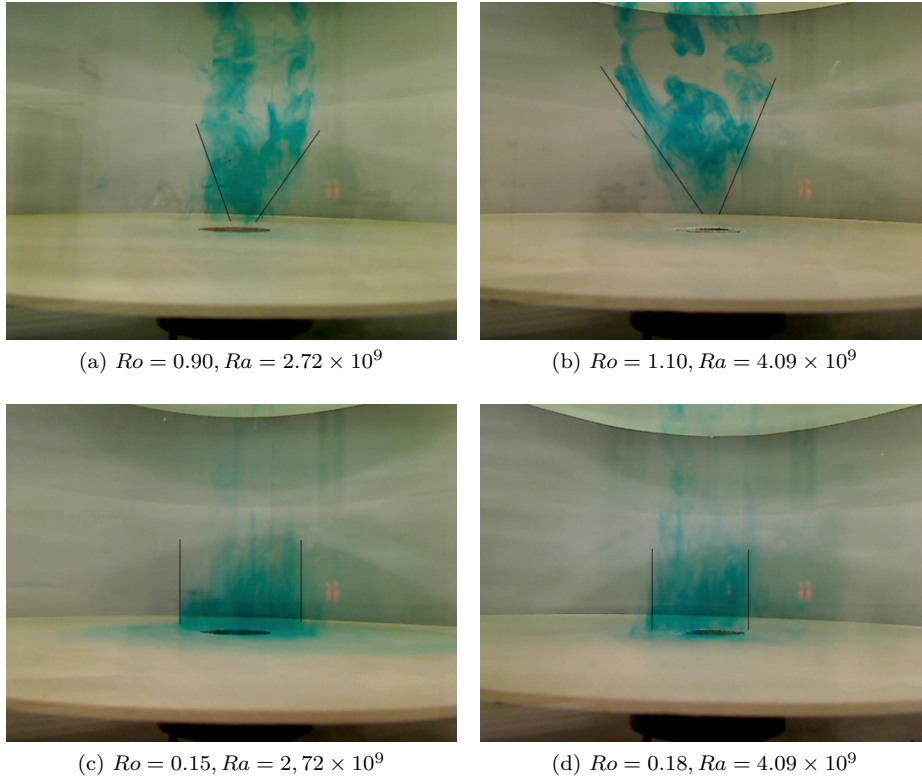
(d) $Ro = 0.18, Ra = 4.09 \times 10^9$

Figure 4.3: Dye visualisation snapshots at various Rayleigh and Rossby numbers.

When the diameter of this column is then measured several times during the experiment, the diameter can be calculated and compared to other diameters.

The calculated diameter is based on 10 snapshots of the same experiment. Two examples of snapshots that are used for this calculation are showed in the Figures 4.3c and 4.3d. For the case where $Ra = 2.72 \times 10^9$ and $Ro = 0.15$ the average diameter is 9 ± 1 cm. The error band given in this result, and in all coming results, is the standard deviation. If this result is expressed in dimensionless form normalised by the diameter of the disc $d_c^* olumn$ this gives a result of $d_c^* olumn = 1.8 \pm 0.2$. When $Ra = 4.09 \times 10^9$ and $Ro = 0.18$ the average diameter is 7.9 ± 0.7 cm. If this value is converted to dimensionless form the result is $d_c^* olumn = 1.6 \pm 0.1$ From this data there can be concluded that the diameters vary significantly as a function of the Rayleigh number.

The simulations and experimental results are compared based on the Rossby number. This means that the simulation with a certain Rossby number is compared with an experiment with the same Rossby number. But first the simulations are mutually compared. Dr. Kamp provided simulations at Rossby numbers of 0.32, 0.16, 0.08, 0.03 and 0.02. All these simulations are made at a

(a) $Ro = 0.30, Ra = 2.72 \times 10^9$ (b) $Ro = 0.28, Ra = 4.07 \times 10^9$

(c) $Ro = 0.30, Ra = 2.72 \times 10^9$ (d) $Ro = 0.28, Ra = 4.07 \times 10^9$
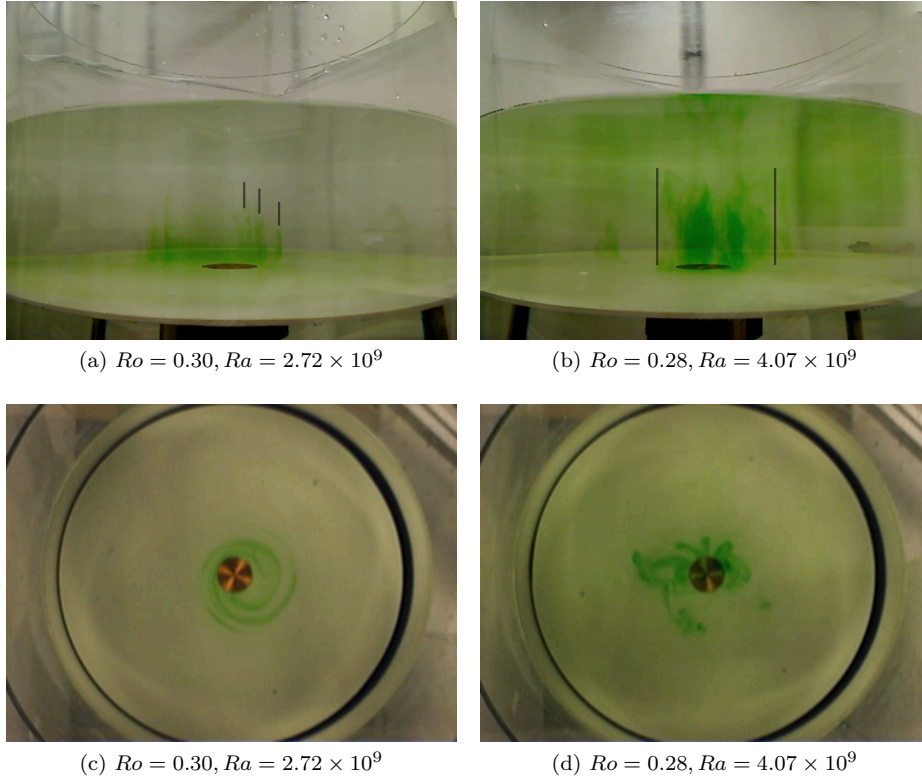
Figure 4.4: Snapshots of the experiments to compare them to the numerical simulations. The black lines are guides to the eye to emphasize the plumes.

Rayleigh number of 1.36×10^9 and presented in Figure 4.5. The coloured background indicates the temperature at that point and the black lines are streamlines for the r-z-flow inside the fluid. One half of the heating disc is displayed on the bottom line between the left corner and the square. The temperature range is between 293.15 K and 298.15 K in which the blue colour represents the colder fluid and the red colour represents the hotter fluid.

From the numerical simulations it can be concluded that when the Rossby number decreases, the number of vertical columns increases. The simulation with the highest Rossby number, which is 0.32, has still a Rossby number that is too low to conclude that in the regime $Ro \approx 1$ a conical shape appears. Another fact is that at lower Rossby numbers, more plumes come to existence. These plumes are axisymmetrical and hollow and hot fluid rises on the inner side and cooler fluid sinks on the outer side of one plume.

There are only 2 simulations that can be used to compare with experiments. These are the simulations with $Ro = 0.32$ and with $Ro = 0.16$. The experimental results that have an approximate equal Rossby number are, at $Ra = 2.72 \times 10^9$, $Ro = 0.30$ and $Ro = 0.15$. At $Ra = 4.07 \times 10^9$ the experiments with $Ro = 0.28$

and $o = 0.18$ can be used. The snapshots of the two lowest Rossby numbers are already provided in Figure 4.3. The snapshots of the highest two Rossby numbers are shown in Figure 4.4

First look at $Ro = 0.32$. In the simulation are two plumes of streamlines. In Figure 4.4a the plumes as can be observed are highlighted using black lines above them. Here there are three plumes. The view from above can be seen in Figure 4.4c. In this figure there are no complete concentric circles but there is a shell structure visible above the heating disc. This result is identified in many snapshots in this particular experiment. In Figure 4.4b there are no plumes to be detected at all. There is only one plume with a region of lesser dye in the middle. This result is confirmed by the view from above in Figure 4.4d.

Now look at Ro=0.16. The snapshots of these experiments are shown in Figure 4.6. In the numerical simulation there are again several plumes with decreasing height towards the edge of the heating disc. In Figure 4.6a only two plumes are visible. This result is confirmed by the view from above in Figure 4.6c where a shell structure can be identified. In the experiment with $Ro = 0.18$ and $Ra = 4.07 \times 10^9$ no plumes can be identified.

These deviations from the numerical simulations are most likely due to several reasons.

- The assumptions that are made with making this simulation are not realistic. In the experiment axial symmetry is broken,

- The simulations are calculated with a different temperature difference than the experimental results.
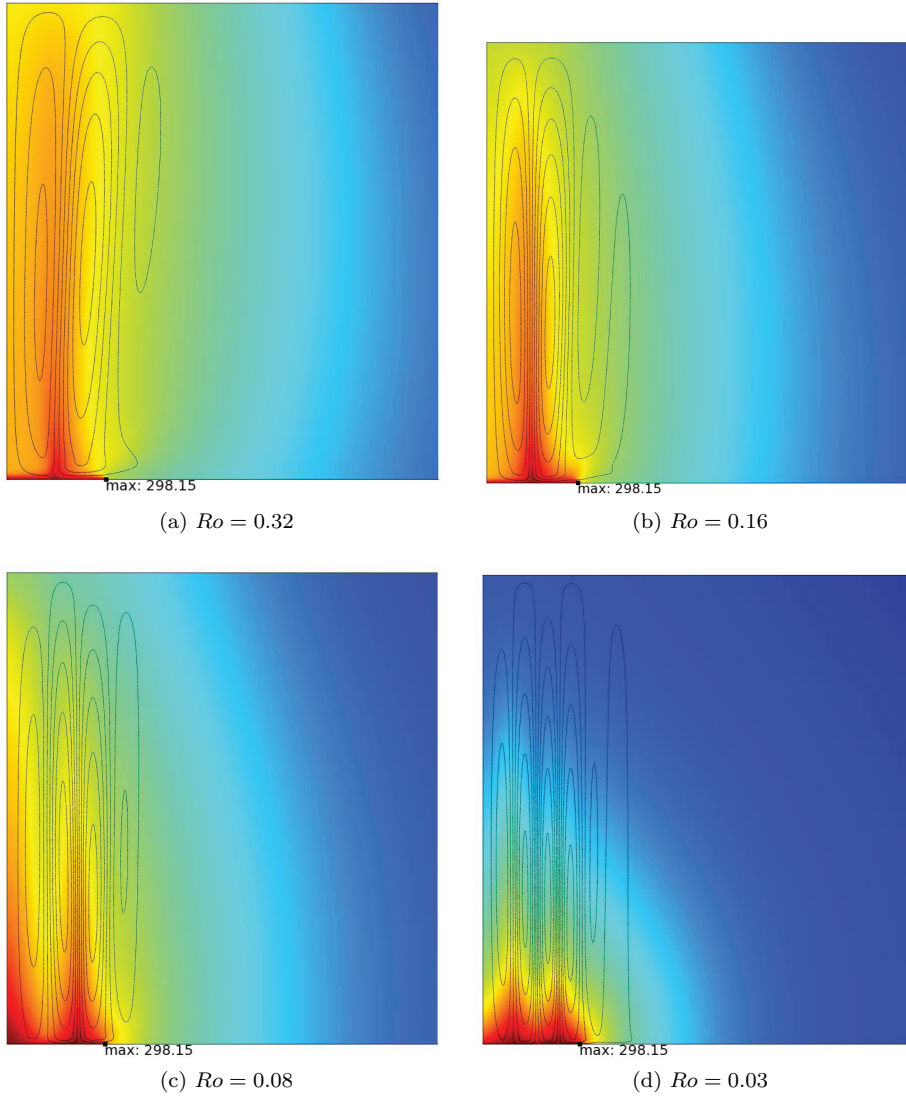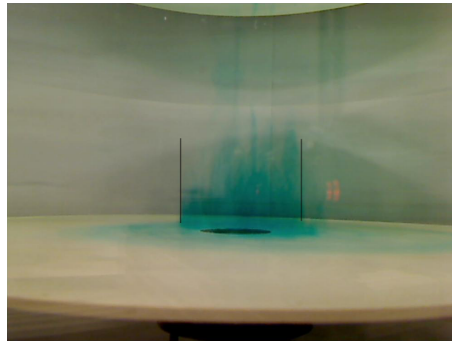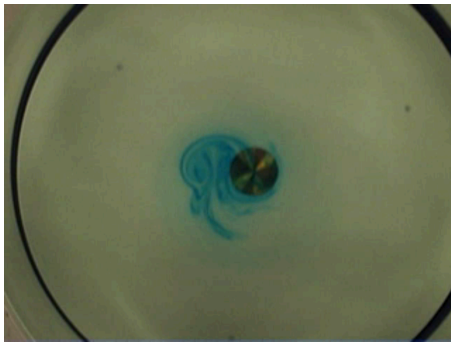
17

(a) $Ro = 0.32$ (b) $Ro = 0.16$

(c) $Ro = 0.08$ (d) $Ro = 0.03$

Figure 4.5: Temperature distribution(colored background) and stream-lines(black lines) from azially symmetric numerical simulations at $Ra = 1.36 \times 10^9$ and various Ro. The left-hand side of the figure coincides with the rotation axis, the right-hand side is the sidewall.
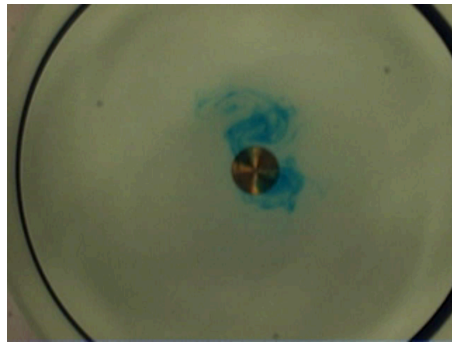
(a) $Ro = 0.15, Ra = 2.72 \times 10^9$

(b) $Ro = 0.18, Ra = 4.07 \times 10^9$

(c) $Ro = 0.15, Ra = 2.72 \times 10^9$

(d) $Ro = 0.18, Ra = 4.07 \times 10^9$

Figure 4.6: Snapshots of the experiments to compare them to the numerical simulations. The black lines are guides to the eye to emphasize plumes or the cylindrical vortex.

Chapter 5

Conclusion

In this last chapter several conclusions will be drawn from the preceding results. These conclusions concern the different regimes of flow in the fluid as a function of the angular frequency of the background rotation and as a function of the temperature difference between the heating disc and the surrounding fluid. First the different flow regimes at different angular frequencies have been considered. These regimes are governed by the Rossby number and are divided into 2 regimes. First there is the regime $Ro \ll 1$ in which the background rotation dominates the buoyancy and tends to make the flow pattern columnar. This is already discussed in depth in Chapter 4. The second region of interest is where $Ro \gg 1$, in which the background rotation can be ignored and the flow pattern is approximately equal to the situation when there is no background rotation. The region of transition lies at $Ro \approx 1$ when the coriolis and buoyancy forces are approximatly equal in magnitude. the forces due to heating.

From the series of measurements at both $Ra = 2.72 \times 10^9$ and $Ra = 4.07 \times 10^9$ the conclusion can be drawn that the transition point between two regimes is temperature dependent. At $Ra = 2.72 \times 10^9$ the transition point lies at $Ro \approx 0.9$ and at $Ra = 4.07 \times 10^9$ this point lies at $Ro \approx 1.0$. This conclusion is backed by the observation that both the conical shape and the cylindrical vortex are present in the experiments at those Rossby numbers.

Next the case of equal angular frequencies but different temperature gradient. This gives the influence of the temperature on the size of the characteristic phenomena at each regime. It was found that at $Ro = 0.15$ and $Ra = 2.72 \times 10^9$ the dimensionless diameter of the columnar vortex equals 1.8±0.2. At $Ro = 0.18$ and $Ra = 4.07 \times 10^9$ this dimensionless diameter is 1.6 ± 0.1. Based on this information it can be concluded that the size of the Taylor column depends on the temperature difference between heating plate and surrounding fluid. If this difference is larger, the size of the column will be smaller. The same holds for the conical shape above the heating plate when looking at $Ro \approx 1$. From the experimental results it can be stated that this cone is sharper at larger temperature differences.

The experimental results are also compared to simulations done by dr.

Kamp. These simulations are made at $Ra = 1.36 \times 10^9$ and so these numerical simulations are compared to situations where the Rossby numbers are equal but the Rayleigh number in the simulations was lower than in the experiments. Experiments at $Ra = 1.36 \times 10^9$ are found to be unsuitable for dye visualisation with visual inspection due to the low flow velocities. The outcome of the comparison between the numerical simulations and the experimental results is that the simplifications made in the simulation are unrealistic. The numerical simulations do, however, sometimes predict the flow pattern correctly.

To conclude this chapter it is useful to look forward to future research. There are several options to further study this subject. It is possible to improve the simulations by considering a three-dimensional flow instead of using the unrealistic assumption of axial symmetry. Other improvements concern the experimental setup. To better monitor the temperatures of the heating disc and the surrounding fluid additional thermometers can be placed in the fluid and heating disc. Another upgrade would be the use of more sophisticated measuring techniques like, for example, particle image velocimetry. The last possible improvements mentioned here are measurements at more Rayleigh numbers, and at more Rossby numbers to further map the transition between the two regimes.

Bibliography

[1] Arnfield, A.J., Two decades of urban climate research: a review of turbulence, exchanges of energy and water, and the urban heat island. *Int. J. Climatol.* **23**, 1-26 (2003).

[2] Myrup, L.O., A Numerical Model of the Urban Heat Island. *J. Appl. Meteor* **8**, 908-918 (1969).

[3] Oke, T.R., Canyon geometry and the nocturnal urban heat island: Comparison of scale model and field observations. *J. Climatol.* **1**, 237-254 (1981).

[4] Boussinesq, J.V. *Théorie Analytique de la Chaleur*, volume 2. Gauthier-Villars, Paris (1903).

[5] Kundu, P.K., Cohen, I.M. *Fluid mechanics*. Academic Press (2008).

[6] Ekman, V.W., On the influence of the earth's rotation on ocean currents. *Ark. Mat. Astron. Fys.* **2** (11), 1-52 (1905).

[7] Hough, S.S., On the Application of Harmonic Analysis to the Dynamical Theory of the Tides. Part I. On Laplace's 'Oscillations of the First Species,' and on the Dynamics of Ocean Currents. *Proc. R. Soc. A.* **61**, 236-238 (1897).

[8] Taylor, G.I., The motion of a sphere in a rotating liquid. *Proc. R. Soc. A.* **102**, 180-189 (1922).

[9] Kunnen R.P.J., *Turbulent rotating convection*, Ph.D. thesis Eindhoven University of Technology (2008).